DROP-IT

DELIVERABLE 4.2

Interfacing of B-LFPs with charge transport layers

Due date of deliverable: 2021/04/30

Actual submission date: 2022/07/13

Deliverable number:	D4.2
Due date:	30.04.2021
Nature[1]:	Report
Dissemination Level[1]:	PU
Work Package:	WP4
Lead Beneficiary:	INSA RENNES
Contributing Beneficiaries:	All

[1] **Nature:** R = Report, P = Prototype, D = Demonstrator, O = Other
Dissemination level PU = Public PP = Restricted to other programme participants (including the Commission Services) RE = Restricted to a group specified by the consortium (including the Commission Services) CO = Confidential, only for members of the consortium (including the Commission Services) Restraint UE = Classified with the classification level "Restraint UE" according to Commission Deci-sion 2001/844 and amendments Confidential UE = Classified with the mention of the classification level "Confidential UE" according to Commission Decision 2001/844 and amendments Secret UE = Classified with the mention of the classification level "Secret UE" according to Commis-sion Decision 2001/844 and amendments

This project has received funding from the European Union's Horizon 2020 research and innovation programme under **Grant Agreement No. 862656**.

Table of Content

This project has received funding from the European Union's Horizon 2020 research and innovation programme under **Grant Agreement No. 862656**.

DROP-IT report
Interfacing of B-LFPs with charge transport layers

PREFACE

Following our first-stage review on the status and future of Lead-free perovskites (LFPs), it is agreed that a competitive evaluation of their development should be provided for, and the photovoltaic performance would be revised accordingly with the help of structural hence electronic improvements. As described in TASK 4.1, the interface of most promising G-LFPs (polycrystalline/nanoparticulated films) in terms of bandgap, electro-optical properties, stability and processability, with selected charge transport layers is studied. Within this report, **a preliminary literature survey of LFPs aimed at selecting charge transport layers** for inkjet printing application, experimental **investigations on interfacing selected transporting layers with LFPs and a computational methodology to address interface modelling are presented** sequentially. **Based on the literature survey and experimental studies from the consortium, we choose the $FASnI_3$ (FA=Formamidine) as the active absorber layer.** Combining experimental and theoretical results, C_{60} which is the analog electron transport layer (ETL) to fullerene derivatives appears as an optimum ETL choice. The detailed theoretical work consists of two parts and is carried out with the SIESTA DFT code, suitable for modeling heterostructures containing hundreds of atoms at a reasonable computational cost. **First, the $FASnI_3$ slabs are computed along the (001) direction** (as the most energetically favorable direction viewed during crystal growth [1]) **with different surface terminations** and investigating the dependence of physical and electronic properties on slab thickness..

This project has received funding from the European Union's Horizon 2020 research and innovation programme under **Grant Agreement No. 862656**.

This project has received funding from the European Union's Horizon 2020 research and innovation programme under **Grant Agreement No. 862656**.

1 Litterature survey of the most appropriate charge transport layers on interfacing with B-LFPs (Sn based)

Organic-inorganic halide perovskites have been studied extensively in electronics and optoelectronics over the last decade [2,3]. Their unique and attractive optoelectronic properties, such as tunable bandgap, strong optical absorption, charge carrier long diffusion length and lifetime and solution processibility [4–6], have guaranteed their versatile applications in solar cells, LEDs, photodetectors and beyond [7–9]. The continuous research effort in compositional and structural explorations of Pb-based perovskite solar cells (PSCs) contributes to their rapid increase of maximum achieved light to electricity conversion efficiency from the initial value of 3.81% [10] to the current value of 25.6% (certified 25.2%) [11]. However, the toxicity of Pb, combined with the difficulty in upscaling and poor stability during solar cell operation are important obstacles for their commercialization [12–14]. To address the problems of unsatisfied stability and severe toxicity of Pb halide perovskites, Pb-free perovskites, formed by substituting Pb^{2+} with, for example, Sn^{2+} in 3D cubic structures, In^{3+}, Bi^{3+}, Sb^{3+}, Ag^{+} mixtures in double perovskite structures, Sn^{4+}, Ti^{4+} in vacancy-ordered structures and Bi^{3+}, Sb^{3+} in 2D-layered structures, have been considered as promising candidates because of their lower toxicity and relatively higher stability [15–17]. For a Pb-free perovskite-based optoelectronic device, its performance is strongly dependent on the charge transport ability when interfacing with the electron and hole transport layers (ETL and HTL). Having proper energy level alignment at perovskites/charge transport layer interfaces is credited for achieving simultaneously enhanced charge collection efficiency and open-circuit voltage of the device. **Figure 1** shows the schematic of valence and conduction energy level (E_V and E_C) values of the most representative Pb and Pb-free perovskites at different types of structures as well as ETLs and HTLs. These values are extracted from

This project has received funding from the European Union's Horizon 2020 research and innovation programme under **Grant Agreement No. 862656**.

experimental and theoretical studies [18–47]. Overall, the bandgaps increase going from I to Br to Cl accompanied by the upshifting E_V and downshifting E_C. Meanwhile, the 3D Sn perovskites have narrower bandgaps and upper E_V and E_C compared to their Pb counterparts. This upshifted E_V and E_C affect the charge transport from themselves to HTLs and ETLs. For example, the $FASnI_3$ has the E_V and E_C of -5.34 eV and -4.12 eV respectively. Its electron transport to C_{60} (E_C = -4.30 eV) is favorable and its hole transport to NiO (E_V = -5.40 eV) is, however, unfavorable considering the high chance of electron-hole recombination at the interfaces. We see from **Figure 1c** that, unlike the 3D Pb-free perovskites, the double, vacancy-ordered and 2D-layered Pb-free perovskites have relatively broader bandgaps and less attractive interface energy level alignments with respect to the most often used ETLs, hampering photovoltaic conversion efficiencies. In addition, due to different types of perovskite surface terminations, the charge collection can change substantially as they are associated with charge transport materials. For instance, the surface of $MAPbI_3$ favors electron transport to C_{60} when it is terminated with an MAI layer, in contrast, impedes electron transport to C_{60} when it is terminated with a PbI_2 layer (see **Figure 1a**). Therefore, in this work, our goal is to choose appropriate ETL and HTL and investigate the effect of perovskite surface terminations on charge transport properties at the HTL/Pb-free perovskites/ETL interfaces, for the purpose of promoting Pb-free perovskites in the optoelectronic application.

Up to now, among all possible Pb-free perovskite (LFP) candidates, Sn-based perovskites alongside their surface and interface functionalization with the assembly of charge transport layers (CTLs) are considered promising ways to achieve a win-win between environmental friendliness and cell performance [48–50]. Indeed, the record of solar cell efficiency for a Pb-free material is obtained by an Sn-based material [11]. As such Sn-based perovskites hold great prospects in achieving similar or even higher photovoltaic properties

This project has received funding from the European Union's Horizon 2020 research and innovation programme under **Grant Agreement No. 862656**.

than their Pb-based counterparts because of their broader absorption range and higher charge carrier mobility [51]. For instance, the comparatively small bandgap of $FASnI_3$ (FA = Formamidinium), namely, 1.41 eV, makes it potentially attractive for near-infrared region harvesting, which is almost unique by comparison to standard perovskites [52]. To date, the short-circuit currents of the best performing Sn-based perovskites can be reasonably compared to the Shockley-Queisser limit. However, their open-circuit voltages exhibit a large deficit to that limit, indicating efficient carrier generation and collection but high non-radiative recombination [53]. Efforts in Sn-based perovskites have been devoted to improving film qualities and eliminating structural and electronic mismatches hence interfacial energy barriers between themselves and CTLs [54]. Meng *et al.* [1] improve the surface-controlled growth of $FASnI_3$ films by adding pentafluorophen-oxyethylammonium iodine (POEI) to lower surface energy. The highly oriented and smooth $FASnI_3$-POEI film gives an efficiency of 10.16% in contrast to the 6.93% of pure $FASnI_3$ film. At the Sn-based perovskite/CTL interface, a suitable energy level alignment is the prerequisite for an efficient photovoltaic device. Since Sn-based perovskites have upshifted conduction and valence band edges compared to Pb-based ones, an inferior electron and hole transport is expected when facing most common CTLs [55,56]. Surface and interface engineering, such as passivating surfaces to improve crystallinity as shown by Nishimura *et al.* [57] or coating $FASnI_3$ with phenylethylammonium bromide to form a dipolar interlayer as introduced by Liao *et al* [58], contribute to the optimization of charge transport between perovskite and electron transport layers (ETLs) thus improving the device performances and slowing down its degradation [59–63]. To date, a record efficiency of 13.24% of Sn-based perovskite is obtained by using C_{60} as the ETL [57] because of the improved interface band alignment. Also, Boehm et al. [64] have discussed the influence of surface ligand on the frontier electronic energy levels across $FASnI_3/C_{60}$ interface by combining ultraviolet, inverse, and X-ray photoelectron

This project has received funding from the European Union's Horizon 2020 research and innovation programme under **Grant Agreement No. 862656**.

spectroscopy. All the above endeavors have focused on improving photoconversion efficiency (PCE), optimizing device optimization and exploring new fabrication methodology, which is all directly related to the surface and interface engineering of perovskites with the assembly of ETLs.

Currently, except for the C_{60} ETL, numerous n-type metal oxides such as TiO_2 [10], SnO_2 [65], ZnO [66], etc. have been explored as ETLs. Among them, TiO_2 is most often used in PSCs, especially in most high efficient PSCs including the current record efficiency holder (i.e., 25.6%) [11]. Unfortunately, under illumination, the poor photic stability and charge carrier mobility of TiO_2, especially for the mesoporous-TiO_2 scaffold, have constrained its long-term usage in solar devices [67]. Besides, its requirement for the high-temperature process becomes a huge burden for the manufacturers considering its high production cost. Therefore, other alternative n-type metal oxides are also developed despite the high performance by using TiO_2. SnO_2 has a wider bandgap [68], higher transparency [69] in the visible light region and better photic stability than the TiO_2. Moreover, SnO_2 is the only one like TiO_2 which can be both used as compact layers and mesoporous layers in solar devices. But, no matter in dye-sensitized solar cells (DSSC) [70] or PSCs [71], SnO_2 based solar cells have a relatively lower efficiency compared to TiO_2 based ones. Facing this, ZnO, because of its low-temperature process which is unlike TiO_2 [72], and similar wide-bandgap to SnO_2 [73], has become the most investigated ETL except for TiO_2. However, its low-cost manufacturing and high transparency in the visible light region do not make up its thermal instability under air ambiance. This instability comes from the fact that during the low-temperature process, the -OH residue on the ZnO surface will cause the decomposition of perovskite layers. [74] **Table 1** lists the functional layers of different LFP based solar cells at their highest PCEs achieved to date. As it shows, the choices of ETLs with respect to different Pb-free perovskite materials are quite limited. The majority ETLs used are C_{60} and/or its derivative such as [6,6]-phenyl-C_{61}-butyric

This project has received funding from the European Union's Horizon 2020 research and innovation programme under **Grant Agreement No. 862656**.

acid methyl ester (PCBM). For a TiO_2 LFP based solar cell, the yielding efficiency is far below its C_{60} counterpart.

For solar cell applications, the PCE achieved to date for any of the double perovskites $A_2BB'X_6$, vacancy ordered double perovskites A_2BX_6 or 2D perovskite derivatives $A_3B_2X_9$, is below 4% and thus far away from the 25.8% achieved with Pb-based halide perovskites[75]. In fact, Tin-based Iodides $ASnI_3$ compositions are the most promising with a current record reaching 14.6%[76]. They also allow room for improvements given that the predicted theoretical limit for thicklayers under AM1.5G illumination for stannates is as high as 32.3%[77]. The materials are less stable than their Pb-based counterparts when subjected to ambient conditions due to the fast Sn^{2+} oxidation. **Within the DROP-IT consortium, a remarkable improvement was achieved recently with over 1300h of operational stability in N_2, with maximum power point (MPP) tracking thanks to chemical engineering by combining addition of a secondary ammonium salt with that of an effective reducing agent[78]**. Specifically, Dipropylammonium iodide together with a well-known reducing agent, sodium borohydride (NaBH4), aimed at preventing the premature degradation of Sn-based devices. Similarly, the highest reported PCEs of $CsSnI_3$ and $MASnI_3$ till now are 12.96%[79] and 7.78%[80], respectively, although it is proven theoretically that their PCEs are limited to 32.3% by comparison to 30.5% for lead-based solar cells[77]. The much lower stability of Sn-based perovskite solar cells by comparison to Pb based ones even when encapsulated, led to the exploration of surface passivation strategies[81].

This project has received funding from the European Union's Horizon 2020 research and innovation programme under **Grant Agreement No. 862656**.

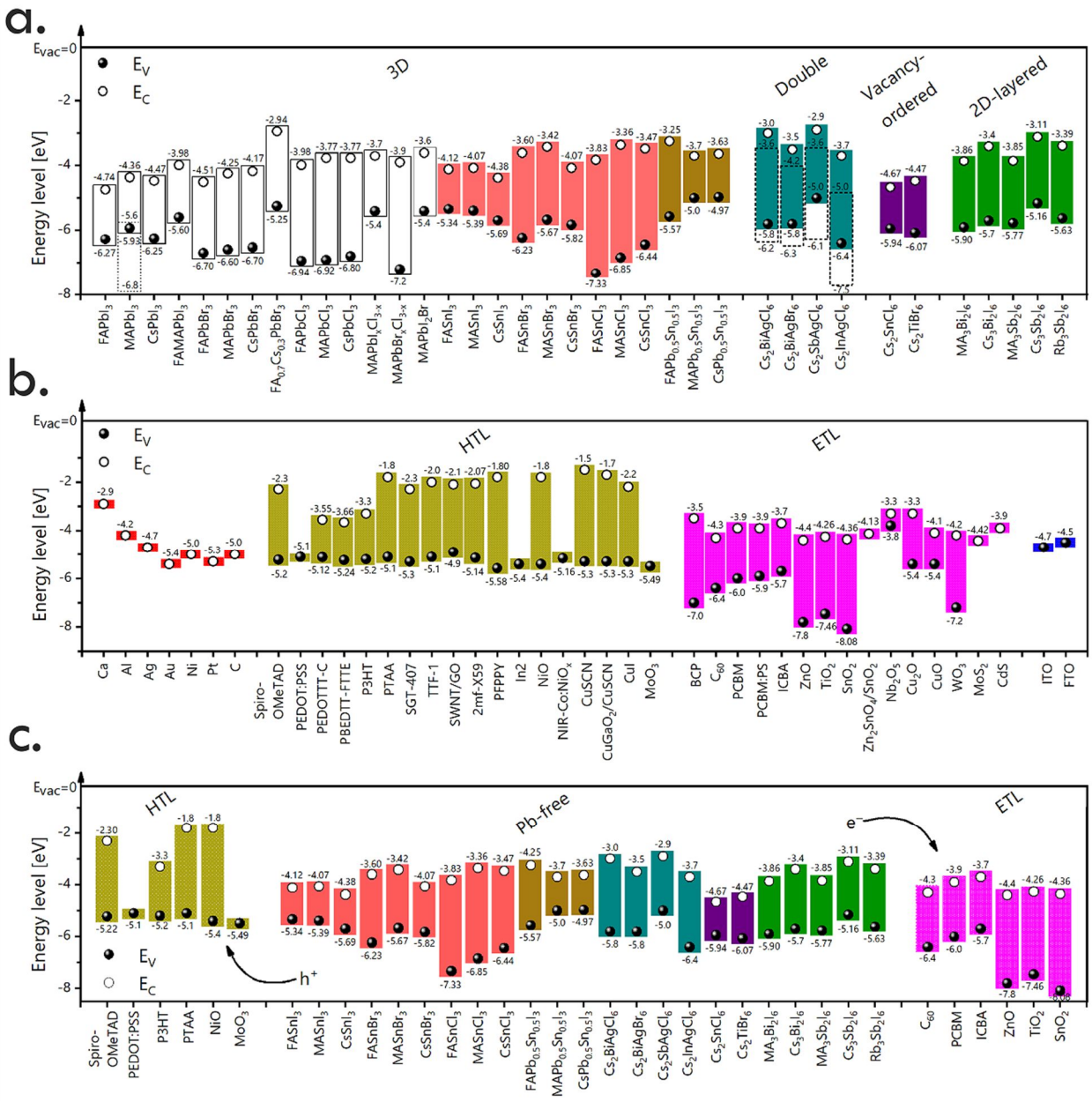

Figure 1. Schematic of energy level alignments of the representative conventional 3D, double, vacancy-ordered double and 2D-layered Pb and Pb-free perovskites (a), charge transport and extraction interlayers (b), and the most often studied HTL/Pb-free perovskites/ETL configurations. HTL and ETL represent hole (h^+) and electron (e^-) transport layers. The dotted blocks represent

This project has received funding from the European Union's Horizon 2020 research and innovation programme under **Grant Agreement No. 862656**.

perovskites at BX_2 or $BX/B'X_3$ (B = Pb, Sn, Bi, Ag, Sb, In; X = I, Br, Cl) surface terminations. All data shown here are extracted from experimental and theoretical study [18–47].

Table 1. Preparation methods of selected Pb-free perovskites based solar cells with thehighest yielding photoconversion efficiency PCE. The open-circuit voltage V_{OC}, short-circuit current J_{SC} and fill factor FF are included as well.

Preparation method	Functional layer	V_{OC} [V]	J_{SC} [mA/ cm^2]	FF [%]	PCE [%]
Spin-coating	ITO/PEDOT:PSS/$MASnI_3$/PCBM/Ag	0.57	20.68	66	7.78 [80]
Spin-coating	FTO/Cu-NiO_x/$FASnI_3$/PCBM/BCP/Ag	0.69	21.15	74	10.9 [82]
Spin-coating + SnF_2	ITO/PEDOT:PSS/$FA_{0.75}MA_{0.25}SnI_3$/C_{60}/BCP/Al	0.55	24.3	67	9.06 [83]
Spin-coating + GeI_2	FTO/PEDOT:PSS/$(FA_{0.9}EA_{0.1})_{0.98}EDA_{0.02}SnI_3$/$C_{60}$/BCP/Ag/Au	0.84	20.32	78	13.24 [57]
Spin coating + FAI/SnI_2/SnF_2	ITO/PEDOT:PSS/$FASnI_3$/C_{60}/BCP/Ag	0.63	21.22	75	10.1 [84]
Spin-coating	ITO/TiO_2/$CsSnI_3$ (QR)/spiro-OMeTAD/Au	0.86	23.2	65	12.96 [79]
Solid-state reaction	FTO/PCBM/$CsSn_{0.5}Ge_{0.5}I_3$/spiro-OMeTAD/Au	0.63	18.41	61	7.11 [85]
Spin-coating + GeI_2/SnF_2	FTO/PEDOT:PSS/$FA_{0.75}MA_{0.25}SnI_3$/PCBM/C_{60}/BCP/Ag/Au	0.45	25.58	69	7.90 [86]
Spin-coating	FTO/bl-TiO_2-/mp-TiO_2/$FASn(I_{0.75}Br_{0.25})_3$/Spiro-OMeTAD/Au	0.41	19.8	67	5.5 [87]

This project has received funding from the European Union's Horizon 2020 research and innovation programme under **Grant Agreement No. 862656**.

2 Experimental realization of various $FASnI_3$ interfaces and devices

Following the literature survey and the internal discussions among partners involved in WP4, UJI proposed a systematic study of Tin-based solar cells using $FASnI_3$ as an absorber. 4 selected different ETLs, all promising in terms of band alignments for carrier extraction were used namely ZnO, ZnO/C_{60}, PCBM and C_{60} as explained below in the experimental procedure.

2.1 Experimental procedure

ITO coated glass where chemically etched with zinc powder and HCl (6M) to obtain the desired ITO pattern, followed by a sequential washing process with soap-water, ethanol, acetone, and isopropanol, respectively, in an ultrasonic bath for 15 min each. Then, the substrates were dried with N_2 flow and subsequently introduced in an UV-Ozone lamp for 20 min. The PEDOT:PSS solution was filtered with 0.45 µm PVDF filter and spin coated on top of ITO at 5,000 rpm (2,000 rpm of acceleration) for 40 s and annealed at 130 ^oC for 20 min in ambient conditions. After the HTL deposition the substrates were introduced in a N_2-filled glovebox, for the $FASnI_3$ layer deposition. The perovskite layer was deposited by one-step method with an antisolvent-based method, by adding $FASnI_3$ precursor solution on top of PEDOT:PSS and spin coated at 4,000 rpm for 50 s. Then 400 µL of chlorobenzene were dropped on top of the substrate after 20 s of spinning, followed by a two-step annealing at 70 ^oC for 1 min and at 100 ^oC for 19 min. After the perovskite layer, a different ETL (C_{60}, PCBM, ZnO or ZnO/C_{60}) was deposited as follow:

- C_{60}: A 30 nm layer was thermally evaporated.

This project has received funding from the European Union's Horizon 2020 research and innovation programme under **Grant Agreement No. 862656**.

- PCBM: A solution of 20 mg/ml dissolved in Chlorobenzene, was spin coated at 2000 rpm for 30s and annealed at 70 °C for 10 min.

-ZnO: Zinc Oxide nanoparticle ink solution dispersed in IPA (Sigma Aldrich), was spin coated at 2000 rpm for 30s and annealed at 70 °C for 10 min.

-ZnO/C_{60}: Zinc Oxide nanoparticle ink solution dispersed in IPA (Sigma Aldrich), was spin coated at 2000 rpm for 30s and annealed at 70 °C for 10 min. Then 30 nm of C_{60} was thermally evaporated.

After the ETL deposition, a 6 nm layer of BCP and 100nm of Ag were thermally evaporated.

2.2 Results and Analysis

The V_{OC}, J_{SC}, FF, and PCE are shown on **Figure 2**. In addition, forward scan J-V curves of $FASnI_3$ champion devices using the 4 ETLs are displayed on **Figure 3**. The analysis reveals that C_{60} compared to PCBM, ZnO/C_{60} and ZnO provides the best characteristics in term of V_{OC}, J_{SC}, FF, and PCE. The short circuit courrents of the ZnO/C_{60} and ZnO based devices are limited, which is pointing toward a lack of efficiency charge extraction. Therefore, despite favorable band alignements, the interface quality with ZnO has a detrimental effect on the device performances, even when ZnO is combined with C_{60}. The device based on PCBM yield more sizeable short circuit current values, but not as high as the ones for the case of C_{60}. This might be partly attributed to less favorable band alignementwith $FASnI_3$ (see figure 1 and Section I). Moreover, the reproducibility of the process used for PCBM is more limited than for C_{60} as shown by the larger dispersion of the experimental J_{SC} values spread over about 10mA.cm². From the perspective of electron extraction, C_{60} appears as the optimum corresponding to state of the art current values. From Table 1 in section, the two champion

This project has received funding from the European Union's Horizon 2020 research and innovation programme under **Grant Agreement No. 862656**.

devices reported with C_{60} and PCBM correspond to efficiencies of about 10.1%[84] and 10.9%[82]. The main target for further device optimization is therefore the low open circuit voltage which is less than 0.4V in our case against more than 0.6V in two champion devices from the litterature. The non-optimized V_{OC} is a very well-known limitation of Sn-based solar cells, by comparison to their lead-based counterparts. Among the various phenomena discussed in the literature (see the recent paper by DROP IT partner[78]) and leading to experimental low V_{OC}, the presence of trap states that originated from the oxidation of Sn +2 to Sn +4 is nowadays a classical explanation. Limiting this oxidation related to the bulk properties of Sn-based materials appears as a crucial step toward solar cell device performances, on par with Pb-based ones.

In the following part of this report, the $FASnI_3$ and C_{60} have been chosen as the absorber and ETL to further investigate at the atomic level the physical and electronic properties considering both the external surfaces and buried interfaces.

This project has received funding from the European Union's Horizon 2020 research and innovation programme under **Grant Agreement No. 862656**.

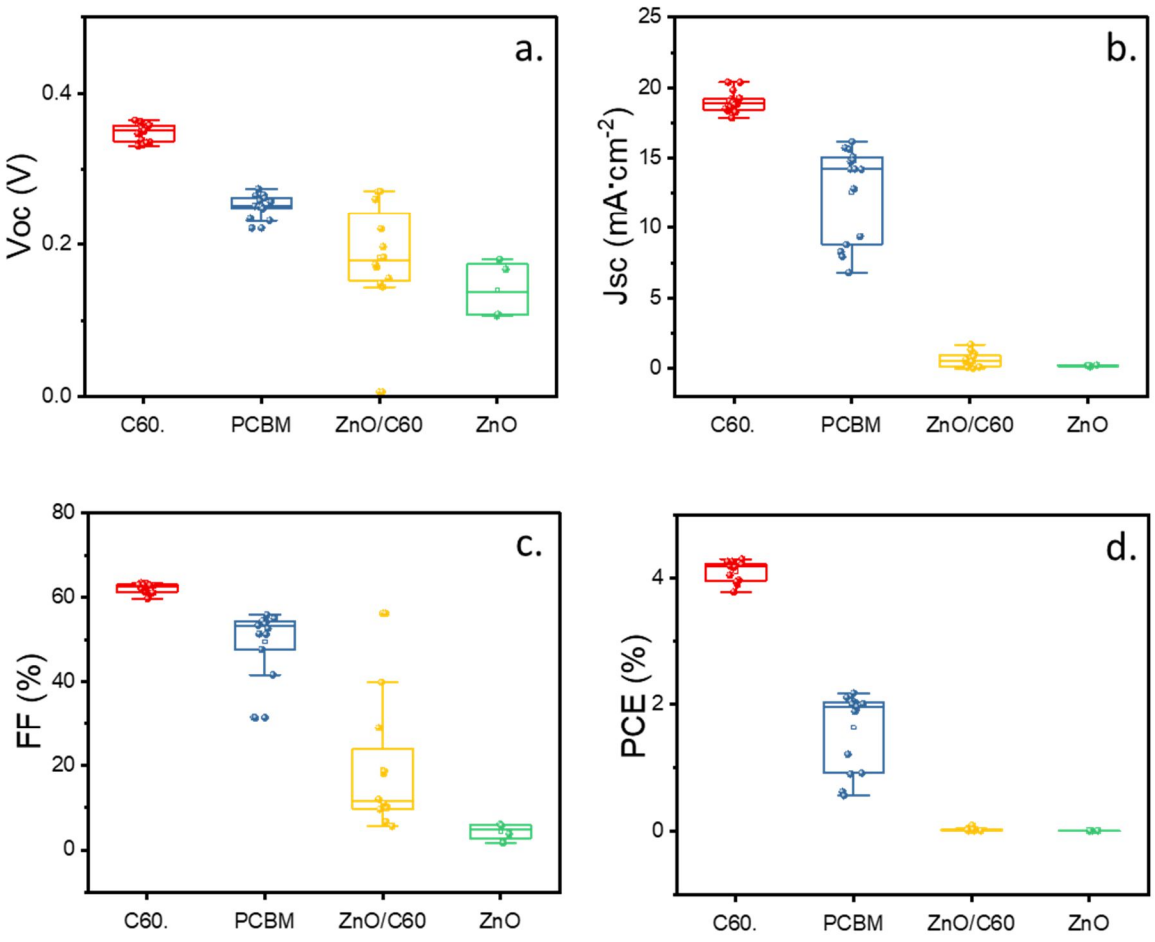

Figure 2. Statistics of the $FASnI_3$ based devices with different electron transport layers, where a. shows Open circuit voltage, b. current density, c. Fill factor and d. Efficiency.

This project has received funding from the European Union's Horizon 2020 research and innovation programme under **Grant Agreement No. 862656**.

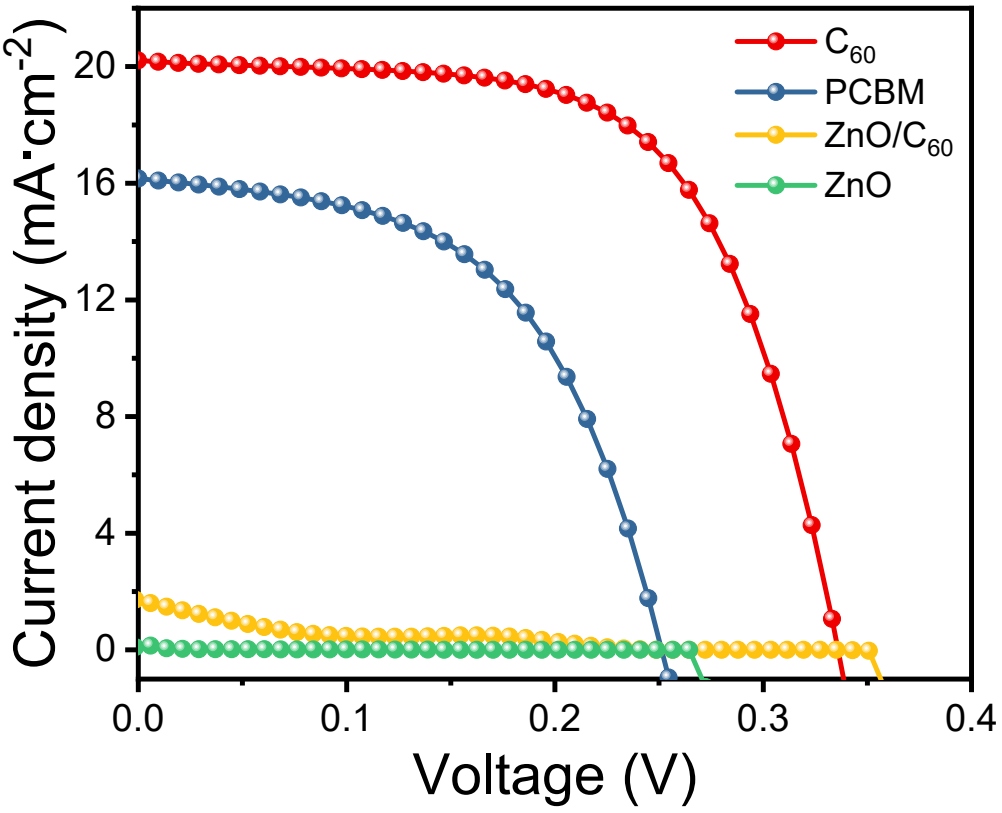

Figure 3. Forward scan J-V curves of $FASnI_3$ champion devices using different electron transport layers.

Table 2. Parameters corresponding to the J-V curves on Figure 3.

ETL	V_{oc} [V]	J_{sc} [mA/ cm^2]	FF [%]	PCE [%]
C_{60}	0.336	20.38	62.76	4.29
PCBM	0.251	16.16	53.72	2.18
ZnO/C_{60}	0.271	1.69	17.97	0.082
ZnO	0.167	0.23	3.81	0.0015

This project has received funding from the European Union's Horizon 2020 research and innovation programme under **Grant Agreement No. 862656**.

3 Detailled theoretical methodology developped for the $FASnI_3/C_{60}$ case

3.1 Materials and Methods

At room temperature, the bulk $FASnI_3$ and C_{60} are in face-center cubic space phases. The theoretical calculations are performed using the SIESTA [88,89] package, which has been implemented within the DFT and also with a basis set of finite-range of numerical atomic orbitals. The DFT calculations have been carried out with the generalized gradient approximation (GGA) functional in the Perdue-Burke-Ernzerhof (PBE) form [90] Troullier–Martins pseudopotentials [91], and a basis set of finite-range numerical pseudoatomic orbitals for the valence wave functions [92]. In addition, $1s^1$, $2s^22p^2$, $2s^22p^3$, $5s^25p^5$, and $5s^24d^{10}5p^2$ were used as valence electrons for H, C, N, I and Sn respectively. For lattice comparison, the van der Waals functional of Dion *et al*. [93] with exchange modified by Cooper [94] (VDW-C09) has been applied for the bulk lattice comparison to GGA-PBE functional. Facing the severe bandgap underestimation at the GGA-PBE level, a recently developed DFT-1/2 method [95,96] is also applied with the ambition to achieve more accurate bandgaps but less demanding computational resources. This DFT-1/2 method removes half an electron from the valence band top and places it to the conduction band bottom, yielding correct ionization energy therefore a better bandgap approximation. .

. ***Slab structures*.** The $FASnI_3$ (001) slabs are modeled at different numbers of octahedral layers (nL) considering both SnI_2-terminated and FAI-terminated surfaces with a 2×2 in-plane periodicity. ***Heterostructures*.** The $FASnI_3/C_{60}$ heterostructure is modeled by assembling the $FASnI_3$ (001) slab at a 2×2 in-plane periodicity with the C_{60} (001) slab at a 1×1 in-plane periodicity, as shown in **Figure 2-4**. For SnI_2-C60 bonding, C atoms from the C60 side

This project has received funding from the European Union's Horizon 2020 research and innovation programme under **Grant Agreement No. 862656**.

are placed on top of Sn atoms, I atoms, and voids between them from the $FASnI_3$ side respectively, which are simplified as “topSn”, “topI” and “topvo”. In the same way, for FAI-C60 bonding, C atoms from the C60 side are placed on top of FA atoms, I atoms and voids between them from the $FASnI_3$ side respectively, which are simplified as “topFA”, “topI” and “topvo”.

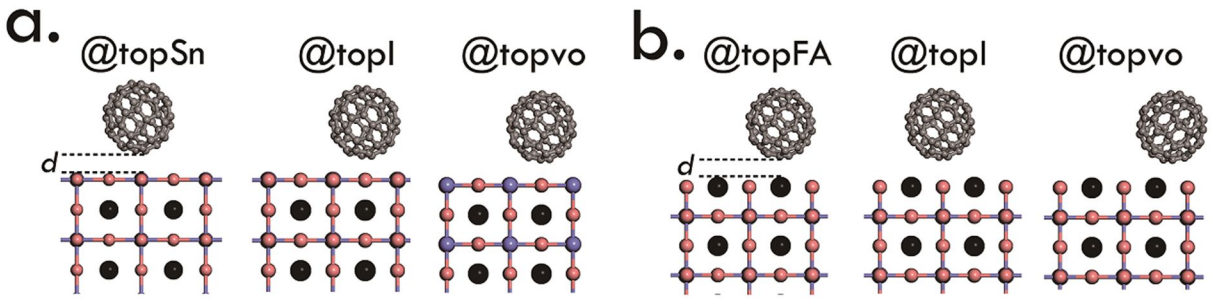

Figure 2-4. Schematics of the $FASnI_3$ (001)/C_{60} (001) heterostructures with (a) SnI_2-C_{60} interfacial bonding @topSn, @topI, @topvo stacking patterns respectively and with (b) FAI-C_{60} interfacial bonding @topFA, @topI, @topvo stacking patterns respectively. Atoms in grey, pink, blue and black represent elements C, I, Sn, and FA^{PS} respectively.

3.2 Physical and electronic properties characterization

3.2.1 Slab stability

The thermodynamic stabilities of SnI_2-terminated and FAI-terminated slabs are evaluated by the differences in energy (ΔE) between one $FASnI_3$ stoichiometry unit in the slabs ($E_{FASnI_3}^{SnI_2}$ at SnI_2-termination; $E_{FASnI_3}^{FAI}$ at FAI-termination) and in the bulk (E_{bulk}). The number of octahedral layers (nL) is used to represent the slab thickness. Because of the surface truncation, the chemical formulae of SnI_2-terminated and FAI-terminated slabs are

This project has received funding from the European Union’s Horizon 2020 research and innovation programme under **Grant Agreement No. 862656**.

not with perfect multiples of one $FASnI_3$ unit, which are $FA_mSn_{m+4}I_{3m+8}$ and $FA_{m+4}Sn_mI_{3m+4}$ respectively, where m equals 4 times the slab thickness, i.e, $m = 4nL$. Therefore, an excess of either $4SnI_2$ or 4FAI units is found for either SnI_2-terminated or FAI-terminated slab. In order to directly compare the values of ΔE between both surface terminations, the total electronic energy of the excess units (namely, $4 \times E_{SnI_2}$ at SnI_2-termination and $4 \times E_{FAI}$ at FAI-termination) need to be subtracted from the parenting slab (namely, $E_{slab}^{SnI_2}$ at SnI_2-termination and E_{slab}^{FAI} at FAI-terminationA negative ΔE means that the modeled slab is thermodynamically stable. The higher the absolute value of ΔE, the more stable the slab.

The surface energy (σ) is used to measure the preference of slab formation under different experimental conditions, which is expressed as

$$\sigma = \frac{1}{2A}\left(E_{slab} - \sum_{x=FA,Sn,I} N_x \mu_x^{slab} - TS + PV\right) \quad (3)$$

where N_x and μ_x^{slab} are the number and chemical potential of each type of entity in the slab, respectively, and A is the surface area. P, V, T and S are pressure, volume, temperature and entropy, respectively. (5)

To prevent the $FASnI_3$ (001) slab from spontaneously breaking into energetically more favored compounds, the chemical potential of the compound in a stable slab should be lower than that in its bulk phase, reading $\mu^{slab} < \mu^{bulk}$. The higher the absolute value of σ, the easier the surface formation.

3.2.2 Heterostructure stability

The work of adhesion (W_{ad}) is used to determine the preferential adsorption site when the C_{60} molecule in its *fcc* lattice approaches the $FASnI_3$ surface,

$$W_{ad} = \left(E_{FASnI_3/C_{60}}^{hetero} - E_{FASnI_3}^{slab} - E_{C_{60}}^{slab}\right)/2A \quad (7)$$

This project has received funding from the European Union's Horizon 2020 research and innovation programme under **Grant Agreement No. 862656**.

where $E_{FASnI_3/C_{60}}^{hetero}$, $E_{FASnI_3}^{slab}$ and $E_{C_{60}}^{slab}$ are the total energies of the $FASnI_3/C_{60}$ heterostructure, and its isolated $FASnI_3$ slab and C_{60} slab respectively, A is the interfacial area, and the 2 is because of the symmetric top and bottom surfaces.

3.2.3 Energy level alignments

As proposed by Kleinman [97], in a semi-infinite crystal, planarly averaging the potential along the direction normal to slab surface (here in the *z*-direction) rules out the contribution of potential from neighboring slabs, thus giving a correct work function W_F . The corresponding vacuum level (E_{vacuum}) can be used as a reference while processing the absolute energy level alignment [98]. By planarly averaging Hartree potential profiles (V_H^{slab}) of a $FASnI_3$ slab as well as that of bulk $FASnI_3$ (V_H^{bulk}), we obtain the absolute valence band edge (E_V) after aligning V_H^{bulk} to V_H^{slab} at the bulk-like interior part with a value of ΔV_H ($= V_H^{slab} - V_H^{bulk}$),

$$E_V = E_{VBM}^{bulk} + \Delta V_H + \Delta E_{vacuum} \quad (8)$$

where E_{VBM}^{bulk} is the VBM of bulk $FASnI_3$ and ΔE_{vacuum} is the vacuum level shift. The absolute conduction band edge (E_C) is obtained by combining the E_V value and the experimental bandgap E_g of bulk $FASnI_3$,

$$E_C = E_V + E_g \quad (9)$$

Similarly, by planarly averaging Hartree potential profiles of the $FASnI_3/C_{60}$ heterostructure ($V_H^{FASnI_3/C_{60}}$) and of the isolated $FASnI_3$ slab ($V_H^{FASnI_3}$) and C_{60} slab ($V_H^{C_{60}}$), we obtain the valence (VBO) and conduction band offsets (CBO) from the following two equations:

$$VBO = \left(E_{VBM}^{FASnI_3} + V_H^{FASnI_3/C_{60}} - V_H^{FASnI_3}\right) - \left(E_{VBM}^{C_{60}} + V_H^{FASnI_3/C_{60}} - V_H^{C_{60}}\right) \quad (10)$$

This project has received funding from the European Union's Horizon 2020 research and innovation programme under **Grant Agreement No. 862656**.

and,

$$CBO = VBO + E_g^{FASnI_3} - E_g^{C_{60}} \quad (11)$$

where $E_{VBM}^{FASnI_3}$ and $E_{VBM}^{C_{60}}$ are VBMs of the isolated $FASnI_3$ slab and C_{60} slab respectively, $E_g^{FASnI_3}$ and $E_g^{C_{60}}$ are experimental bandgaps of bulk $FASnI_3$ and C_{60} taken from references [52] and [99] respectively, and $\Delta V_H = V_H^{FASnI_3/C_{60}} - V_H^{FASnI_3}$ (or $V_H^{C_{60}}$) are used to align the V_H of the isolated $FASnI_3$ (or C_{60}) slabs to the heterostructures.

3.2.4 Link between work function and surface dipole

There is a link between the work function and the surface dipole. According to the definition of the displacement electric field:

$$D = \epsilon_0 E + P \quad (12)$$

where ε_0 is the permittivity in a vacuum, E is the electric field and P is the polarization density that captures the field due to "trapped" dipole moments. Comparing the divergence of Eq. (12) to Gauss's law, we have $\rho_b = -\nabla \cdot P$ where $\rho_b = \rho_{b_{eletronic}} + \rho_{b_{ionic}}$ is the bound charge density comprising of both electronic and ionic parts.

For each modeled $FASnI_3$ slab, we obtain its surface dipole density p by

$$p = \int_{z_0}^{c/2} P_z(z) dz. \quad (13)$$

From Leung et al. [100], the surface dipole and the work function are related within the framework of local density approximation formulation. The change of work function $\Delta W_F = \Delta\phi$ is unambiguously consistent with the change of the dipole moment Δp *via* the equation below,

$$\Delta\phi = -e\frac{\Delta p}{\epsilon_0} = -1.809 \times 10^{-8}\Delta p \quad (14)$$

where ϕ is in J, charge e is in C, ϵ_0 is in F/m and p is in C/m.

This project has received funding from the European Union's Horizon 2020 research and innovation programme under **Grant Agreement No. 862656**.

4 THEORETICAL RESULTS AND DISCUSSION

4.1 $FASnI_3$ and C_{60} bulk materials

The lattice parameters $a\ (= b = c)$, bandgaps (E_g) and bulk moduli (B_0) of room temperature (RT) face-centered cubic (*fcc*) $FASnI_3$ and C_{60} [101,102] are listed in **Table 3-1**. For $FASnI_3$, due to its fast re-orientational motion of FA cation and in order to fulfill the average RT lattice symmetry, a fictitious atom "FA^{PS}" (where "PS" refers to the use of a pseudo-atom and the associated pseudopotential) has been developed in our group, to mimic the effective cation size in the perovskite cage [103,104]. As listed in **Table 3-1**, the lattice parameters obtained from such procedure using the GGA-PBE level of theory [90] match better with the RT experimental values than what is obtained from the VDW-C09 level of theory [94], while the E_g obtained from both functionals are underestimated. Given the E_g underestimation, a recently developed DFT-1/2 method [105] has been chosen to simultaneously achieve better bandgap accuracy and low computational cost instead of the hybrid functionals or even more demanding many-body corrections, which are not affordable for large heterostructures. **Figure 3-1** compares the band structures of bulk $FASnI_3$ and C_{60} at GGA-PBE and DFT-1/2 level of theory. We see that the bandgap of $FASnI_3$ at the GGA-PBE level stays direct at the "R" *k*-point for the DFT-1/2 calculation, but its value has been expanded by exhibiting a 491 meV downshift of the valence band maximum (VBM) and a 538 meV upshift of the conduction band minimum (CBM). Similarly, the direct bandgap of C_{60} at the GGA-PBE level has been expanded by the DFT-1/2 method with a 117 meV downshift of the VBM and a 203 meV upshift of the CBM. **Figure 3-2** plots the band structures of bulk $FASnI_3$ and C_{60} considering the spin-orbit coupling (SOC) effect. Unlike the negligible SOC effect of C_{60}, $FASnI_3$ has a sizeable spin-orbit splitting located at the CBM. The

This project has received funding from the European Union's Horizon 2020 research and innovation programme under **Grant Agreement No. 862656**.

corresponding bandgap shrinkage of $FASnI_3$ (around 0.4 eV) agrees well with Tao *et al*. [106] and Umari *et al*. [107]. Considering the severe bandgap underestimation of $FASnI_3$ under the GGA-PBE+SOC calculation, we select the following three levels of theory in our subsequent surface and interface calculations, namely, GGA-PBE for structural minimization, DFT-1/2 and DFT-1/2+SOC for electronic structure calculations.

Table 3-1. Lattice parameters $a\ (= b = c)$, electronic bandgaps (E_g) and bulk moduli (B_0) of cubic $FASnI_3$ and C_{60} in this work at different levels of theory using DFT and comparison to RT (unless specified) experimental results and other DFT-based theoretical results. In the present work, a pseudo-atom FA^{PS} is used to mimic the effective FA cation size in the perovskite cage at RT.

	Functional	**$FASnI_3$**			**C_{60}**		
		a [Å]	E_g [eV]	B_0 [GPa]	a [Å]	E_g [eV]	B_0 [GPa]
This work	GGA-PBE	6.31	0.50	21.13	13.97	1.19	32.43
	GGA-PBE+SOC		0.11	-		1.20	-
	DFT-1/2		1.53	-		1.51	-
	DFT-1/2+SOC		1.14	-		1.51	-
	VDW-C09	6.15	0.19	-	13.82	1.14	-
Exp.		6.32 (300 K)[108] 6.30 (275 K)[101]	1.41[52] 1.38[64] 1.34[109]	-	14.15[110] 14.20[102] 14.26[111]	2.13[64] 1.70[99] 1.70[112]	14.7[113] 14.0[114]
Cal.		6.44[115] 6.40[116]	0.96[115] 0.70[116] 1.40[106]	12.96[117] 15.10[118]	13.19[119]	2.15[120] 2.12[121] 1.66[122]	-

This project has received funding from the European Union's Horizon 2020 research and innovation programme under **Grant Agreement No. 862656**.

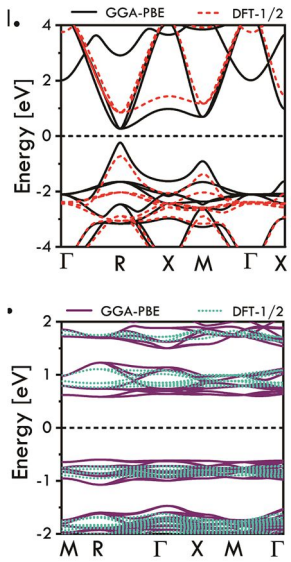

Figure 3-1. Electronic properties at GGA-PBE and DFT-1/2 level of theory: (top) band structures of bulk $FASnI_3$; (bottom) band structures of bulk C_{60}. The Fermi level is set to zero eV.

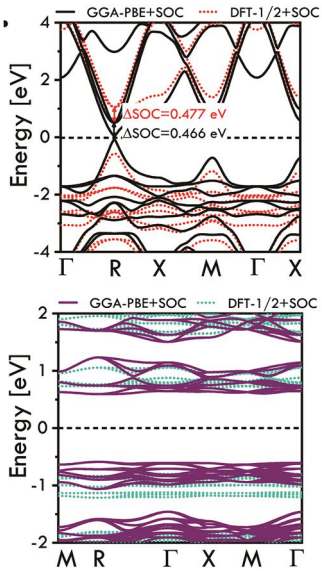

This project has received funding from the European Union's Horizon 2020 research and innovation programme under **Grant Agreement No. 862656**.

Figure 3-2. Electronic properties at GGA-PBE+SOC and DFT-1/2+SOC level of theory: (top) band structure of bulk $FASnI_3$; (bottom) band structure of bulk C_{60}. The Fermi level is set to zero eV. The ΔSOC in (a) means spin-orbit splitting at the CBM.

4.2 Thermodynamic stability at various surface terminations

4.2.1 $FASnI_3$ (001) slab

The SnI_2-terminated and FAI-terminated slabs are thermodynamically stable as shown by the negative values of ΔE (**Figure 3-3a)**. Moreover, the FAI-terminated slabs are energetically more stable than the SnI_2-terminated ones. By increasing the slab thickness from 4L to 14L, $|\Delta E|$ decreases and reaches a convergence around 10L. We can conclude that the slab at the thickness of 10L can be considered from the energetic viewpoint as a composite structure made of a bulk-like interior region plus surface layers. So, the 10L will be taken for the subsequent heterostructure modeling. Note that, the ΔE at DFT-1/2 and DFT-1/2+SOC levels follow the same trend as the ΔE at GGA-PBE level, though their values are more negative regardless of the slab thickness.

Figure 3-3b plots the evolution of σ with respect to the chemical potential difference ($\mu_{SnI_2}^{slab} - \mu_{SnI_2}^{bulk}$). Note that the $\mu_{SnI_2}^{slab} - \mu_{SnI_2}^{bulk}$ is in range of $[\Delta E_f^0; 0]$, where ΔE_f^0 is the formation energy of a bulk structure from a thermodynamics point of view. As it shows, at GGA-PBE, DFT-1/2 and DFT-1/2+SOC levels, the σ of SnI_2-terminated slabs are in between [-19.45; 14.56], [-39.37; 10.10], [-35.01; 11.99] meV/Å^2 respectively and that of FAI-terminated slabs are in between [-40.52; -74.53], [-52.70; -101.84], [-48.47; -95.47] meV/Å^2 respectively. The smaller σ values at FAI-termination in comparison to those at SnI_2-termination indicate that FAI-terminated slabs will be formed preferentially. Besides, when

This project has received funding from the European Union's Horizon 2020 research and innovation programme under **Grant Agreement No. 862656**.

the $\mu_{SnI_2}^{slab} - \mu_{SnI_2}^{bulk}$ is smaller than -3.10 eV at GGA-PBE level (or, -6.22 eV at DFT-1/2 level, -5.57 eV at DFT-1/2+SOC level), SnI_2-terminated slabs will not be formed at all because of positive σ values.

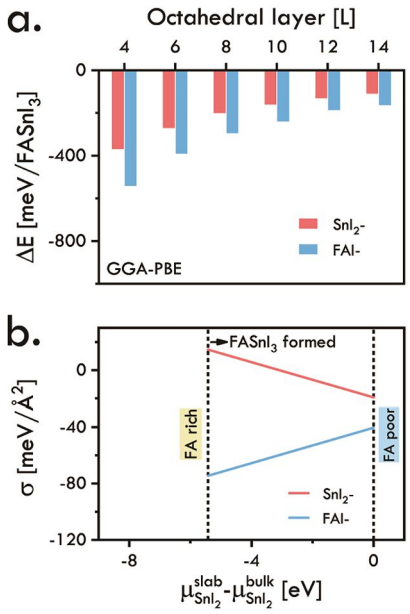

Figure 3-3. Thermodynamical properties of $FASnI_3$ (001) slab at GGA-PBE level of theory respectively: (a) the difference in energy ΔE between $FASnI_3$ unit in the slabs and in the bulk as the slab thickness goes from 4L to 14L; (b) surface energy σ at the converged thickness of 10L as a function of chemical potential difference $\mu_{SnI_2}^{slab} - \mu_{SnI_2}^{bulk}$.

4.2.2 $FASnI_3$ (001)/C_{60} (001) heterostructures

Before proceeding, the interfacial distance *d* is optimized by computing the W_{ad} of a series of unrelaxed heterostructures at a varying *d* [123]. By polynomial fitting this W_{ad} *vs d* to the 4th order, we have the adjusted R-squares (Adj. R^2) over 0.99 for all systems. From these fitted curves, we obtain the optimal interfacial distances (d_{opt}) located at the lowest W_{ad} (written as $W_{ad\_unrelaxed}$), as summarized in **Table 3-2**. The lower value of the

This project has received funding from the European Union's Horizon 2020 research and innovation programme under **Grant Agreement No. 862656**.

$W_{ad\_unrelaxed}$, the higher stability of the heterostructure. So, the stability sequence of SnI_2-C_{60} bonding is @topvo > @topSn > @topI and that of FAI-C_{60} bonding is @topFA > @topvo > @topI. Obviously, SnI_2-C_{60} @topvo and FAI-C_{60} @topFA are the two most stable systems for the respective interfacial bondings. Also, the W_{ad} after relaxing atomic coordination (written as $W_{ad\_relaxed}$) are listed in **Table 3-2**. We see that the $W_{ad\_relaxed}$ have more negative values than $W_{ad\_unrelaxed}$ and follow the same trend as $W_{ad\_unrelaxed}$, except for the opposite values of SnI_2-C_{60} @topSn and SnI_2-C_{60} @topI systems. At all levels of theory, the obtained $W_{ad\_relaxed}$ of SnI_2-C_{60} @topvo have a larger absolute value than that of FAI-C_{60} @topFA, which means that the SnI_2-terminated surface is more favorable for C_{60} adsorption than the FAI-terminated one, although the SnI_2-terminated surface is viewed as less energetically stable in a vacuum than the FAI-terminated one.

Table 3-2. The work of adhesion W_{ad} before and after relaxing atomic coordination (written as $W_{ad\_unrelaxed}$ and $W_{ad\_relaxed}$) at the optimal interfacial distances d_{opt} extracted from **Erreur ! Source du renvoi introuvable.**.

Bonding	Pattern	d_{opt} [Å]	$W_{ad\_unrelaxed}$ [meV/Å^2]	$W_{ad\_relaxed}$ [meV/Å^2]		
			GGA-PBE	GGA-PBE	DFT-1/2	DFT-1/2+SOC
SnI_2-C_{60}	@topSn	3.2	−10.4	−6.3	−14.4	−30.7
	@topI	3.4	−6.3	−8.7	−52.9	−43.7
	@topvo	2.8	−13.2	−16.2	−55.5	−46.8
FAI-C_{60}	@topFA	3.4	−2.0	−5.6	−42.1	−44.9
	@topI	3.4	1.4	−1.1	−23.7	−25.9
	@topvo	3.5	−0.9	−3.5	−27.4	−30.0

This project has received funding from the European Union's Horizon 2020 research and innovation programme under **Grant Agreement No. 862656**.

4.3 Electronic properties at various surface terminations

4.3.1 $FASnI_3$ (001) slab

Figure 3-4 plots the planar averaged Hartree potential profiles (V_H^{slab}) of 10L SnI_2-terminated and FAI-terminated slabs (*as examples*), as well as that of bulk $FASnI_3$ (V_H^{bulk}). From the ΔV_H, we obtain the absolute band edges, see **Figure 3-5**. At the GGA-PBE level, the E_V of SnI_2-terminated slab decreases while that of FAI-terminated slab increases as the slab thickness increases continuously. However, at the DFT-1/2 level, the E_V values for both terminations smoothly decrease. A similar evolution is seen at the DFT-1/2+SOC level (not shown here). The reason for this coinciding prediction comes from the fact that the SOC is negligible at the VBM [124]. An abrupt drop in the E_V is found for the 6L FAI-termination regardless of the levels of theory. In addition, the E_V reaches a convergence at the thickness of 10L as well, which serves as an auxiliary to our previous stability convergence. With respect to slab thickness, the SnI_2-terminated slabs are found to be more sensitive to surface states than the FAI-terminated ones, as proven by their more pronounced band edge variation. A proper guess for the two terminations having dissimilar sensitivities is given by their nonidentical slab stabilities.

Compared to FAI-terminated slabs, the SnI_2-terminated ones have their band edges further away from the E_{vacuum} at the GGA-PBE level while closer to the E_{vacuum} at DFT-1/2 with and without SOC levels. So, the correction of pseudopotentials of Sn and I atoms in the DFT-1/2 method are proven strong enough to substantially divert the relative position of band edges. In particular, at the GGA-PBE level, the difference of E_V between 10L SnI_2-terminated and FAI-terminated slabs ΔE_V ($= E_V^{SnI_2} - E_V^{FAI}$, representing their Coulomb potential difference in a vacuum with respect to the Fermi level) is 0.780 eV, while at DFT-1/2 level, the ΔE_V are -0.641 eV. Here, our DFT-1/2 computed E_V of SnI_2-terminated and FAI-terminated slabs match fairly well with the results from Liao *et al*. [109] and Koh *et al*. [52] respectively. However, as pointed out previously [64], the experimentally reported values for E_V cover a large energy range from -4.7 eV to -6.0 eV [19,52,61,64,109,125] which might be related

This project has received funding from the European Union's Horizon 2020 research and innovation programme under **Grant Agreement No. 862656**.

to different sample preparations or experimental conditions. We may reasonably infer from the present simulations that different surface terminations may play a role in the large dispersion of experimental values.

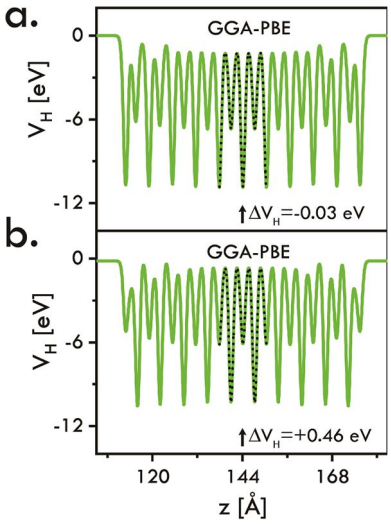

Figure 3-4. Planar averaged Hartree potential profiles V_H of 10L SnI_2-terminated (a) and FAI-terminated (b) slabs along the *z*-direction at GGA-PBE (green lines) level of theory. The ΔV_H is the value used to align the V_H of bulk $FASnI_3$ (dark lines) to that of $FASnI_3$ slabs.

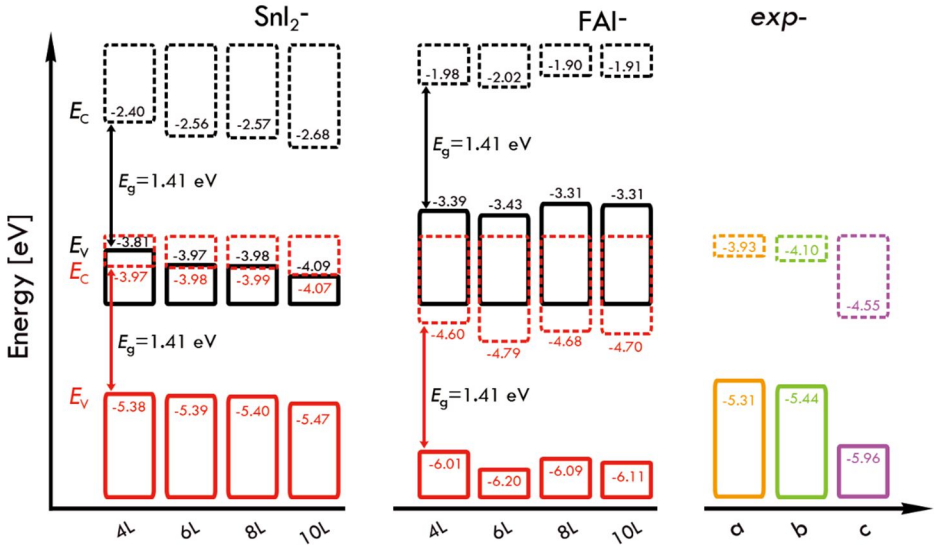

This project has received funding from the European Union's Horizon 2020 research and innovation programme under **Grant Agreement No. 862656**.

Figure 3-5. Absolute valence E_V and conduction E_C band edges of SnI_2-terminated and FAI-terminated slabs from 4L to 10L at GGA-PBE (black blocks) and DFT-1/2 (red blocks) level of theory. The experimental bandgap value of bulk $FASnI_3$ is used from reference [52]. Experimental data *exp-a* (orange blocks), *exp-b* (green blocks) and *exp-c* (purple blocks) are extracted from references [64], [109] and [52] respectively. More experimental data [19,61,125].

To understand the microscopic origin of that large ΔE_V between two terminations, charge distribution and polarization profiles are used for characterizing the changes of work function and surface dipole. **Figure 3-6a-b** plots the planar averaged electron density ($\rho_b^{slab}(z)_{\ eletronic}$ in $e^{\bullet}/Å^3$) of $FASnI_3$ slab at the GGA-PBE level, which points out that the SnI_2-terminated surface is charge concentrated while the FAI-terminated slab is charge deficient, indicating an electron transfer from the FAI- layer to SnI_2- layer at the surface outmost region. This electron transfer brings about a local surface dipole pointing in the opposite direction, which is responsible for the shift of work function $\Delta\phi$, according to Eq. (9). Between two terminations, the difference in their bound charge densities is obtained by $\Delta\rho_b^{slab}(\mathrm{z}) = \rho_b^{SnI_2}(\mathrm{z}) - \rho_b^{FAI}(\mathrm{z})$ (see **Figure 3-6c**). It is found that in slabs the $\Delta\rho_b^{slab}(\mathrm{z})$ mainly occur at the surface areas and they are symmetric with respect to the middle of the bulk-like interior. As a result, the differences in their polarization densities $\Delta P_z^{slab}(z) = P_z{}^{SnI_2}(\mathrm{z}) - P_z{}^{FAI}(\mathrm{z})$ (see **Figure 3-6d**, in C/m^2) will fade away in the bulk-like interior justifying the assumption of vanishing dipoles at $z = z_0$, and they counteract each other at the opposite surface layers.

By integrating the $P_z^{slab}(z)$ using Eq. (13), we obtain the surface dipole moment (p^{slab}, in C/m) and the difference of p^{slab} between two terminations ($\Delta p^{slab} = p^{SnI_2} - p^{FAI}$), as listed in **Table 3-3**. From this Δp^{slab}, the difference of work function between two terminations $\Delta\phi^{slab}$ is achieved using Eq. (14). We find that the values of $\Delta\phi^{slab}$ are in

This project has received funding from the European Union's Horizon 2020 research and innovation programme under **Grant Agreement No. 862656**.

excellent agreement with those of ΔE_V extracted from **Figure 3-5** at GGA-PBE and DFT-1/2 levels. Note that, results at DFT-1/2+SOC level are not shown here. This tells us that the gap of absolute valence band edges between two surface terminations is uniquely due to the shift of their surface dipoles. The agreement between ΔE_V and $\Delta\phi$ not only confirms the proportional relationship between the changes of surface dipole and work function [100], but also underlines the link between surface dipole and energy level alignment, as proposed by our group [126]. Specifically, the Δp^{slab} obtained from GGA-PBE calculation is positive while that obtained from DFT-1/2 calculations is negative. It means that compared to FAI-terminated surface, SnI_2-terminated surface is predicted to have less concentrated surface charges under DFT-1/2 calculation than those under GGA-PBE calculation. This corresponds to the VBM distributions in the insets of **Figure 3-6**, where the SnI_2-terminated surface charges at DFT-1/2 level relocate towards the slab interior part in comparison to those at the GGA-PBE level, meanwhile, the FAI-terminated ones remain evenly distributed around the surface vicinity for all levels of theory.

This project has received funding from the European Union's Horizon 2020 research and innovation programme under **Grant Agreement No. 862656**.

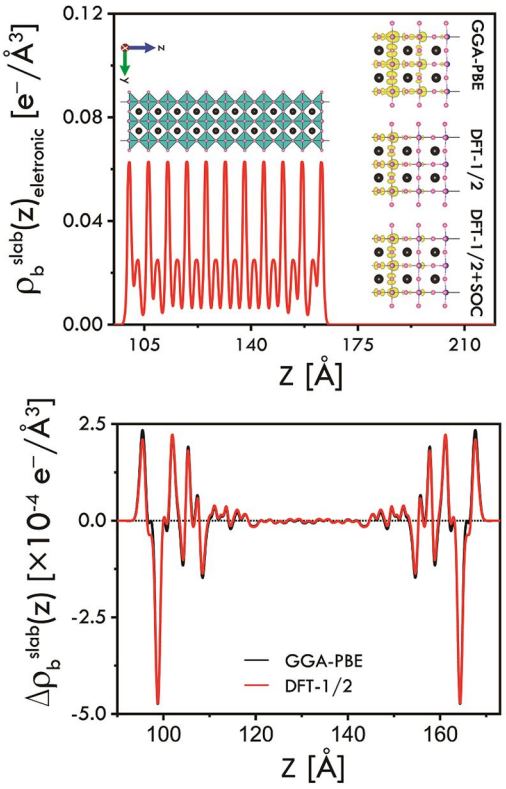

Figure 3-6. Planar averaged electron density profiles $\rho_b^{slab}(z)_{eletronic}$ of 10L SnI_2-terminated (top) slabs along the *z*-direction at the GGA-PBE level of theory. Differences of planar averaged bound charge density $\Delta\rho_b^{slab}(z)$ (bottom) between two terminations at GGA-PBE and DFT-1/2 level of theory. Insets in (top) are VBM distributions near surfaces with an isovalue of 1.5×10^{-4} e$^-$/Å^3 at different levels of theory. Atoms in pink, blue and black represent elements I, Sn, and FA^{PS} respectively.

Table 3-3. Surface dipole moment p^{slab} of 10L SnI_2-terminated and FAI-terminated slabs as well as their differences $\Delta p^{slab} = p^{SnI_2} - p^{FAI}$ at each level of theory. Comparison of the work function differences $\Delta\phi^{slab}$ using Eq. (9) and the absolute valence band edge differences ΔE_V ($= E_V^{SnI_2} - E_V^{FAI}$) extracted from **Figure 3-5.**

Functional	GGA-PBE	DFT-1/2

This project has received funding from the European Union's Horizon 2020 research and innovation programme under **Grant Agreement No. 862656**.

Termination	SnI_2-	FAI-	SnI_2-	FAI-
p^{slab} [×E-11, C/m]	3.564	2.870	3.057	3.628
Δp^{slab} [×E-11, C/m]	0.694		-0.571	
$\Delta\phi^{slab}$ [eV]	0.777		-0.641	
ΔE_V [eV]	0.780		-0.638	

4.3.2 $FASnI_3$ (001)/C_{60} (001) heterostructures

From the planar averaged Hartree potential profiles of the $FASnI_3/C_{60}$ heterostructure and of the isolated $FASnI_3$ slab and C_{60} slab, see **Figure 3-7** where SnI_2-C_{60} @topvo and FAI-C_{60} @topFA are taken as examples. In fact, the $FASnI_3/C_{60}$ heterostructures belong to the type-II interface band alignments with the absolute band edges of $FASnI_3$ higher than those of C_{60}. This tells us that under illumination, the excited electrons in $FASnI_3$ absorbers can transport freely to the C_{60} ETL while the excited holes are blocked from drifting into the C_{60} ETL, yielding a small interfacial electron-hole recombination. This small interfacial recombination proves the wide use of C_{60} as an effective ETL in Pb-free perovskite solar cells [57,64,127]. We observe that the VBOs and CBOs computed by DFT-1/2 and DFT-1/2+SOC are of relatively larger magnitudes than those computed by GGA-PBE, and their values match perfectly with the experimental data from other studies [56,57,99,112] ranging in 0.9-1.2 eV and 0.6-0.9 eV respectively.

This project has received funding from the European Union's Horizon 2020 research and innovation programme under **Grant Agreement No. 862656**.

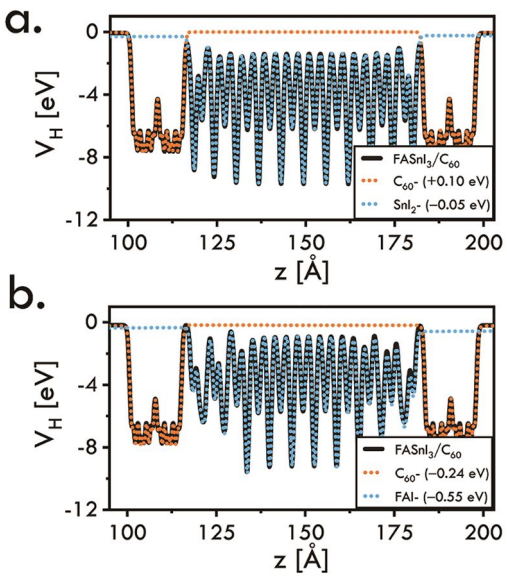

Figure 3-7. Planar averaged Hartree potential profiles V_H of the $FASnI_3/C_{60}$ heterostructures and the isolated $FASnI_3$ slabs and C_{60} slabs with (a) SnI_2-C_{60} @topvo and (b) FAI-C_{60} @topFA interfaces at the GGA-PBE level of theory. Numbers followed behind the components in the legend box are the $\Delta V_H = V_H^{FASnI_3/C_{60}} - V_H^{FASnI_3}$ (or $V_H^{C_{60}}$) used to align the V_H of the isolated $FASnI_3$ (or C_{60}) slabs to the heterostructures.

This project has received funding from the European Union's Horizon 2020 research and innovation programme under **Grant Agreement No. 862656**.

5 GENERAL CONCLUSIONS AND PERSPECTIVES

In this report, **we have presented a literature survey of LFPs aiming at selecting charge transport layers that could be used** for the inkjet printing applications. This survey is **followed by experimental investigations of various $FASnI_3$ devices using selected interfaces**. Finally, a detailed **computational methodology to address atomistic interface modeling by DFT has been developed**.

The DROP IT partners have decided to focus both experimentally and theoretically on $FASnI_3$ /C_{60} heterostructures and devices, which appear as a good compromise in terms of device performances, especially for charge extraction leading to sizeable short circuit current values. The practical Voc limitations have been attributed to oxidation issues, which are specific of Sn-based perovskite bulk properties rather than interface issues. Circumventing these problems as shown by DROP partners **by chemical engineering, combining addition of a secondary ammonium salt with that of an effective reducing agent, shall have in turn beneficial effects on device stability**[78].

This project has received funding from the European Union's Horizon 2020 research and innovation programme under **Grant Agreement No. 862656**.

6 REFERENCES

1. Meng, X. *et al.* Surface-controlled oriented growth of $FASnI_3$ crystals for efficient lead-free perovskite solar cells. *Joule* **4**, 902–912 (2020).
2. Green, M. A., Ho-Baillie, A. & Snaith, H. J. The emergence of perovskite solar cells. *Nat. Photonics* **8**, 506–514 (2014).
3. Li, J. *et al.* Review on recent progress of lead-free halide perovskites in optoelectronic applications. *Nano Energy* **80**, 105526 (2021).
4. Dong, Q. *et al.* Electron-hole diffusion lengths>175 μm in solution-grown $CH_3NH_3PbI_3$ single crystals. *Science* **347**, 967–970 (2015).
5. Green, M. A. & Bein, T. Perovskite cells charge forward. *Nat. Mater.* **14**, 559–561 (2015).
6. Bi, Y. *et al.* Charge carrier lifetimes exceeding 15 μs in Methylammonium lead iodide single crystals. *J. Phys. Chem. Lett.* **7**, 923–928 (2016).
7. Li, X. *et al.* A vacuum flash–assisted solution process for high-efficiency large-area perovskite solar cells. *Science* **353**, 58–62 (2016).
8. Li, B., Long, R., Xia, Y. & Mi, Q. All-inorganic perovskite $CsSnBr_3$ as a thermally stable, free-carrier semiconductor. *Angew. Chem. Int. Ed.* **57**, 13154–13158 (2018).
9. Noel, N. K. *et al.* Lead-free organic–inorganic tin halide perovskites for photovoltaic applications. *Energy Env. Sci* **7**, 3061–3068 (2014).
10. Kojima, A., Teshima, K., Shirai, Y. & Miyasaka, T. Organometal Halide Perovskites as Visible-Light Sensitizers for Photovoltaic Cells. *J. Am. Chem. Soc.* **131**, 6050–6051 (2009).
11. Jeong, J. *et al.* Pseudo-halide anion engineering for α-FAPbI3 perovskite solar cells. *Nature* **592**, 381–385 (2021).

This project has received funding from the European Union's Horizon 2020 research and innovation programme under **Grant Agreement No. 862656**.

12. Feng, J. & Xiao, B. Effective masses and electronic and optical properties of nontoxic $MASnX_3$ (X = Cl, Br, and I) perovskite structures as solar cell absorber: a theoretical study using HSE06. *J. Phys. Chem. C* **118**, 19655–19660 (2014).
13. Berhe, T. A. *et al.* Organometal halide perovskite solar cells: degradation and stability. *Energy Environ. Sci.* **9**, 323–356 (2016).
14. Manser, J. S., Saidaminov, M. I., Christians, J. A., Bakr, O. M. & Kamat, P. V. Making and Breaking of Lead Halide Perovskites. *Acc. Chem. Res.* **49**, 330–338 (2016).
15. Hong, W.-L., Lo, P.-H., Chiu, H.-Z., Horng, S.-F. & Chao, Y.-C. The Influence of Spontaneous Oxidative Conversion on the Characteristics of Lead-Free Halide Perovskite CsSn(IxBr1−x)3 and on the Performance of Perovskite Light-Emitting Diodes. *Adv. Mater. Interfaces* **8**, 2002240 (2021).
16. Eperon, G. E. *et al.* Perovskite-perovskite tandem photovoltaics with optimized band gaps. *Science* **354**, 861–865 (2016).
17. Kim, S.-Y. *et al.* Wide range tuning of band gap energy of A3B2X9 perovskite-like halides. *Scr. Mater.* **166**, 107–111 (2019).
18. Chueh, C.-C., Li, C.-Z. & Jen, A. K.-Y. Recent progress and perspective in solution-processed Interfacial materials for efficient and stable polymer and organometal perovskite solar cells. *Energy Environ. Sci.* **8**, 1160–1189 (2015).
19. Tao, S. *et al.* Absolute energy level positions in tin- and lead-based halide perovskites. *Nat. Commun.* **10**, 2560 (2019).
20. Volonakis, G. & Giustino, F. Surface properties of lead-free halide double perovskites: Possible visible-light photo-catalysts for water splitting. *Appl. Phys. Lett.* **112**, 243901 (2018).
21. Zhang, J. *et al.* Energy barrier at the N719-dye/CsSnI3 interface for photogenerated holes in dye-sensitized solar cells. *Sci. Rep.* **4**, 6954 (2015).

This project has received funding from the European Union's Horizon 2020 research and innovation programme under **Grant Agreement No. 862656**.

22. Yang, F., Kang, D.-W. & Kim, Y.-S. Improved interface of ZnO/$CH_3NH_3PbI_3$ by a dynamic spin-coating process for efficient perovskite solar cells. *RSC Adv.* **7**, 19030–19038 (2017).
23. Kam, M., Zhang, Q., Zhang, D. & Fan, Z. Room-Temperature Sputtered SnO2 as Robust Electron Transport Layer for Air-Stable and Efficient Perovskite Solar Cells on Rigid and Flexible Substrates. *Sci. Rep.* **9**, 6963 (2019).
24. Lee, Y. *et al.* Enhanced charge collection with passivation of the tin oxide layer in planar perovskite solar cells. *J. Mater. Chem. A* **5**, 12729–12734 (2017).
25. Pitchaiya, S. *et al.* A review on the classification of organic/inorganic/carbonaceous hole transporting materials for perovskite solar cell application. *Arab. J. Chem.* **13**, 2526–2557 (2020).
26. Badrooj, M., Jamali-Sheini, F. & Torabi, N. Roles of Sn content in physical features and charge transportation mechanism of Pb-Sn binary perovskite solar cells. *Sol. Energy* **209**, 590–601 (2020).
27. Ran, C. *et al.* Conjugated Organic Cations Enable Efficient Self-Healing FASnI3 Solar Cells. *Joule* **3**, 3072–3087 (2019).
28. Jani, M. R. *et al.* Exploring solar cell performance of inorganic Cs2TiBr6 halide double perovskite: A numerical study. *Superlattices Microstruct.* **146**, 106652 (2020).
29. Cai, R. *et al.* Perovskite Light-Emitting Diodes Based on $FAPb_{1-x}Sn_xBr_3$ Nanocrystals Synthesized at Room Temperature. *IEEE Trans. Nanotechnol.* **18**, 1050–1056 (2019).
30. Zhen, J. *et al.* An ethanolamine-functionalized fullerene as an efficient electron transport layer for high-efficiency inverted polymer solar cells. *J. Mater. Chem. A* **4**, 8072–8079 (2016).
31. Kuan, C.-H., Shen, H.-H. & Lin, C.-F. Low photoactive phase temperature all-inorganic, tin–lead mixed perovskite solar cell. *RSC Adv.* **11**, 3264–3271 (2021).

This project has received funding from the European Union's Horizon 2020 research and innovation programme under **Grant Agreement No. 862656**.

32. Li, F., Wang, Y., Xia, K., Hoye, R. L. Z. & Pecunia, V. Microstructural and photoconversion efficiency enhancement of compact films of lead-free perovskite derivative $Rb_3Sb_2I_9$. *J. Mater. Chem. A* **8**, 4396–4406 (2020).
33. Vigneshwaran, M. *et al.* Facile Synthesis and Characterization of Sulfur Doped Low Bandgap Bismuth Based Perovskites by Soluble Precursor Route. *Chem. Mater.* **28**, 6436–6440 (2016).
34. Bai, F. *et al.* Lead-free, air-stable ultrathin Cs3Bi2I9 perovskite nanosheets for solar cells. *Sol. Energy Mater. Sol. Cells* **184**, 15–21 (2018).
35. Umar, F. *et al.* Dimensionality Controlling of $Cs_3Sb_2I_9$ for Efficient All-Inorganic Planar Thin Film Solar Cells by HCl-Assisted Solution Method. *Adv. Opt. Mater.* **7**, 1801368 (2019).
36. Wang, F. *et al.* Highly stable perovskite solar cells with an all-carbon hole transport layer. *Nanoscale* **8**, 11882–11888 (2016).
37. Gaml, E. A. *et al.* Alternative benzodithiophene (BDT) based polymeric hole transport layer for efficient perovskite solar cells. *Sol. Energy Mater. Sol. Cells* **168**, 8–13 (2017).
38. Yang, S. *et al.* Highly efficient and stable planar CsPbI2Br perovskite solar cell with a new sensitive-dopant-free hole transport layer obtained via an effective surface passivation. *Sol. Energy Mater. Sol. Cells* **201**, 110052 (2019).
39. Lee, P.-H. *et al.* High-efficiency perovskite solar cell using cobalt doped nickel oxide hole transport layer fabricated by NIR process. *Sol. Energy Mater. Sol. Cells* **208**, 110352 (2020).
40. Lee, B. *et al.* Aminosilane-Modified $CuGaO_2$ Nanoparticles Incorporated with CuSCN as a Hole-Transport Layer for Efficient and Stable Perovskite Solar Cells. *Adv. Mater. Interfaces* **6**, 1901372 (2019).
41. Sathiyan, G. *et al.* Dual effective dopant based hole transport layer for stable and efficient perovskite solar cells. *Nano Energy* **72**, 104673 (2020).

This project has received funding from the European Union's Horizon 2020 research and innovation programme under **Grant Agreement No. 862656**.

42. Li, M. *et al.* Doping of [In $_2$ (phen) $_3$ Cl $_6$]·CH $_3$ CN·2H $_2$ O Indium-Based Metal-Organic Framework into Hole Transport Layer for Enhancing Perovskite Solar Cell Efficiencies. *Adv. Energy Mater.* **8**, 1702052 (2018).
43. Chung, J. *et al.* Record-efficiency flexible perovskite solar cell and module enabled by a porous-planar structure as an electron transport layer. *Energy Environ. Sci.* **13**, 4854–4861 (2020).
44. Yokoyama, T. *et al.* Improving the Open-Circuit Voltage of Sn-Based Perovskite Solar Cells by Band Alignment at the Electron Transport Layer/Perovskite Layer Interface. *ACS Appl. Mater. Interfaces* **12**, 27131–27139 (2020).
45. Guo, Y. *et al.* RF sputtered CdS films as independent or buffered electron transport layer for efficient planar perovskite solar cell. *Sol. Energy Mater. Sol. Cells* **178**, 186–192 (2018).
46. Bai, Y. *et al.* High performance inverted structure perovskite solar cells based on a PCBM:polystyrene blend electron transport layer. *J. Mater. Chem. A* **3**, 9098–9102 (2015).
47. Singh, R. *et al.* Perovskite solar cells with an MoS $_2$ electron transport layer. *J. Mater. Chem. A* **7**, 7151–7158 (2019).
48. Lazemi, M., Asgharizadeh, S. & Bellucci, S. A computational approach to interface engineering of lead-free $CH_3NH_3SnI_3$ highly-efficient perovskite solar cells. *Phys. Chem. Chem. Phys.* **20**, 25683–25692 (2018).
49. Pantaler, M. *et al.* Hysteresis-free lead-free double perovskite solar cells by interface engineering. *ACS Energy Lett.* **3**, 22 (2018).
50. Shao, S. & Loi, M. A. The role of the interfaces in perovskite solar cells. *Adv. Mater. Interfaces* **7**, 1901469 (2020).
51. Bai, D. *et al.* ASnX3—Better than Pb-based Perovskite. *Nano Sel.* **2**, 159–186 (2021).

This project has received funding from the European Union's Horizon 2020 research and innovation programme under **Grant Agreement No. 862656**.

52. Koh, T. M. *et al.* Formamidinium tin-based perovskite with low E_g for photovoltaic applications. *J. Mater. Chem. A* **3**, 14996–15000 (2015).
53. Pecunia, V., Occhipinti, L. G., Chakraborty, A., Pan, Y. & Peng, Y. Lead-free halide perovskite photovoltaics: Challenges, open questions, and opportunities. *APL Mater.* **8**, 100901 (2020).
54. Takahashi, Y., Hasegawa, H., Takahashi, Y. & Inabe, T. Hall mobility in tin iodide perovskite $CH_3NH_3SnI_3$: evidence for a doped semiconductor. *J. Solid State Chem.* **205**, 39–43 (2013).
55. Da, P. & Zheng, G. Tailoring interface of lead-halide perovskite solar cells. *Nano Res.* **10**, 1471–1497 (2017).
56. Ke, W., Stoumpos, C. C. & Kanatzidis, M. G. “Unleaded” perovskites: status quo and future prospects of Tin-based perovskite solar cells. *Adv. Mater.* **31**, 1803230 (2019).
57. Nishimura, K. *et al.* Lead-free tin-halide perovskite solar cells with 13% efficiency. *Nano Energy* **74**, 104858 (2020).
58. Liao, Y. *et al.* Highly Oriented Low-Dimensional Tin Halide Perovskites with Enhanced Stability and Photovoltaic Performance. *J. Am. Chem. Soc.* **139**, 6693–6699 (2017).
59. Bai, Y. *et al.* Enhancing stability and efficiency of perovskite solar cells with crosslinkable silane-functionalized and doped fullerene. *Nat. Commun.* **7**, 12806 (2016).
60. Yang, G. *et al.* Interface engineering in planar perovskite solar cells: energy level alignment, perovskite morphology control and high performance achievement. *J. Mater. Chem. A* **5**, 1658–1666 (2017).
61. Liu, C.-K. *et al.* Lead-Free Perovskite/Organic Semiconductor Vertical Heterojunction for Highly Sensitive Photodetectors. *ACS Appl. Mater. Interfaces* **12**, 18769–18776 (2020).
62. Khanal, R., Ayers, N., Banerjee, S. & Choudhury, S. Atomic structure and electronic properties of lead and tin based hybrid halide perovskite surface for photovoltaic applications. *AIP Adv.* **9**, 085123 (2019).

This project has received funding from the European Union’s Horizon 2020 research and innovation programme under **Grant Agreement No. 862656**.

63. Quarti, C., De Angelis, F. & Beljonne, D. Influence of surface termination on the energy level alignment at the $CH_3NH_3PbI_3$ perovskite/C60 interface. *Chem. Mater.* **29**, 958–968 (2017).
64. Boehm, A. M., Liu, T., Park, S. M., Abtahi, A. & Graham, K. R. Influence of surface ligands on energetics at $FASnI_3$/C60 interfaces and their impact on photovoltaic performance. *ACS Appl. Mater. Interfaces* **12**, 5209–5218 (2020).
65. Ke, W. *et al.* Low-Temperature Solution-Processed Tin Oxide as an Alternative Electron Transporting Layer for Efficient Perovskite Solar Cells. *J. Am. Chem. Soc.* **137**, 6730–6733 (2015).
66. Son, D.-Y., Im, J.-H., Kim, H.-S. & Park, N.-G. 11% Efficient Perovskite Solar Cell Based on ZnO Nanorods: An Effective Charge Collection System. *J. Phys. Chem. C* **118**, 16567–16573 (2014).
67. Leijtens, T. *et al.* Overcoming ultraviolet light instability of sensitized TiO2 with meso-superstructured organometal tri-halide perovskite solar cells. *Nat. Commun.* **4**, 2885 (2013).
68. Arlinghaus, F. J. Energy bands in stannic oxide (SnO2). *J. Phys. Chem. Solids* **35**, 931–935 (1974).
69. Joo Yeom, E. *et al.* Controllable synthesis of single crystalline Sn-based oxides and their application in perovskite solar cells. *J. Mater. Chem. A* **5**, 79–86 (2017).
70. Wang, Y.-F., Li, X.-F., Li, D.-J., Sun, Y.-W. & Zhang, X.-X. Controllable synthesis of hierarchical SnO2 microspheres for dye-sensitized solar cells. *J. Power Sources* **280**, 476–482 (2015).
71. Yang, G. *et al.* Effective Carrier-Concentration Tuning of SnO2 Quantum Dot Electron-Selective Layers for High-Performance Planar Perovskite Solar Cells. *Adv. Mater.* **30**, 1706023 (2018).

This project has received funding from the European Union's Horizon 2020 research and innovation programme under **Grant Agreement No. 862656**.

72. Liu, D. & Kelly, T. L. Perovskite solar cells with a planar heterojunction structure prepared using room-temperature solution processing techniques. *Nat. Photonics* **8**, 133–138 (2014).
73. Harun, K., Salleh, N. A., Deghfel, B., Yaakob, M. K. & Mohamad, A. A. DFT + U calculations for electronic, structural, and optical properties of ZnO wurtzite structure: A review. *Results Phys.* **16**, 102829 (2020).
74. Yang, J., Siempelkamp, B. D., Mosconi, E., De Angelis, F. & Kelly, T. L. Origin of the Thermal Instability in CH3NH3PbI3 Thin Films Deposited on ZnO. *Chem. Mater.* **27**, 4229–4236 (2015).
75. Min, H. *et al.* Perovskite solar cells with atomically coherent interlayers on SnO2 electrodes. *Nature* **598**, 444–450 (2021).
76. Jiang, X. *et al.* One-Step Synthesis of SnI2·(DMSO)x Adducts for High-Performance Tin Perovskite Solar Cells. *J. Am. Chem. Soc.* **143**, 10970–10976 (2021).
77. Filippetti, A. *et al.* Fundamentals of tin iodide perovskites: a promising route to highly efficient, lead-free solar cells. *J. Mater. Chem. A* **9**, 11812–11826 (2021).
78. Sanchez-Diaz, J. *et al.* Tin perovskite solar cells with >1,300 h of operational stability in N2 through a synergistic chemical engineering approach. *Joule* **6**, 861–883 (2022).
79. Chen, L.-J., Lee, C.-R., Chuang, Y.-J., Wu, Z.-H. & Chen, C. Synthesis and optical properties of lead-free cesium tin halide perovskite quantum rods with high-performance solar cell application. *J. Phys. Chem. Lett.* **7**, 5028–5035 (2016).
80. Wang, P. *et al.* Ion Exchange/Insertion Reactions for Fabrication of Efficient Methylammonium Tin Iodide Perovskite Solar Cells. *Adv. Sci.* **7**, 1903047 (2020).
81. Li, B. *et al.* Efficient Passivation Strategy on Sn Related Defects for High Performance All-Inorganic CsSnI3 Perovskite Solar Cells. *Adv. Funct. Mater.* **31**, 2007447 (2021).
82. Chen, M. *et al.* High-Performance Lead-Free Solar Cells Based on Tin-Halide Perovskite Thin Films Functionalized by a Divalent Organic Cation. *ACS Energy Lett.* **5**, 2223–2230 (2020).

This project has received funding from the European Union's Horizon 2020 research and innovation programme under **Grant Agreement No. 862656**.

83. Liu, X. *et al.* Solvent engineering improves efficiency of lead-free tin-based hybrid perovskite solar cells beyond 9%. *ACS Energy Lett.* **3**, 2701–2707 (2018).
84. Wu, T. *et al.* Efficient and stable tin-based perovskite solar cells by introducing π-conjugated Lewis base. *Sci. China Chem.* **63**, 107–115 (2020).
85. Chen, M. *et al.* Highly stable and efficient all-inorganic lead-free perovskite solar cells with native-oxide passivation. *Nat. Commun.* **10**, 1–8 (2019).
86. Ng, C. H. *et al.* Role of GeI2 and SnF2 additives for SnGe perovskite solar cells. *Nano Energy* **58**, 130–137 (2019).
87. Lee, S. J. *et al.* Reducing Carrier Density in Formamidinium Tin Perovskites and Its Beneficial Effects on Stability and Efficiency of Perovskite Solar Cells. *ACS Energy Lett.* **3**, 46–53 (2018).
88. Soler, J. M. *et al.* The SIESTA method for *ab initio* order- *N* materials simulation. *J. Phys. Condens. Matter* **14**, 2745–2779 (2002).
89. Artacho, E. *et al.* The SIESTA method; developments and applicability. *J. Phys. Condens. Matter* **20**, 064208 (2008).
90. Perdew, J. P., Burke, K. & Ernzerhof, M. Generalized Gradient Approximation Made Simple. *Phys. Rev. Lett.* **77**, 3865–3868 (1996).
91. Troullier, N. & Martins, J. L. Efficient pseudopotentials for plane-wave calculations. *Phys. Rev. B* **43**, 1993–2006 (1991).
92. Artacho, E., Sánchez-Portal, D., Ordejón, P., García, A. & Soler, J. M. Linear-Scaling ab-initio Calculations for Large and Complex Systems. *Phys. Status Solidi B* **215**, 809–817.
93. Dion, M., Rydberg, H., Schröder, E., Langreth, D. C. & Lundqvist, B. I. Van der Waals Density Functional for General Geometries. *Phys. Rev. Lett.* **92**, 246401 (2004).
94. Cooper, V. R. Van der Waals density functional: An appropriate exchange functional. *Phys. Rev. B* **81**, 161104 (2010).

This project has received funding from the European Union's Horizon 2020 research and innovation programme under **Grant Agreement No. 862656**.

95. Hohenberg, P. & Kohn, W. Inhomogeneous Electron Gas. *Phys. Rev.* **136**, B864–B871 (1964).

96. Kohn, W. & Sham, L. J. Self-Consistent Equations Including Exchange and Correlation Effects. *Phys. Rev.* **140**, A1133–A1138 (1965).

97. Kleinman, L. Comment on the average potential of a Wigner solid. *Phys. Rev. B* **24**, 7412–7414 (1981).

98. Das, T., Rocquefelte, X. & Jobic, S. Ab initio positioning of the valence and conduction bands of bulk photocatalysts: proposition of absolute reference energy. *J. Phys. Chem. C* **124**, 19426–19434 (2020).

99. Lee, M. *et al.* Indene-C60 Bisadduct Electron-Transporting Material with the High LUMO Level Enhances Open-Circuit Voltage and Efficiency of Tin-Based Perovskite Solar Cells. *ACS Appl. Energy Mater.* **3**, 5581–5588 (2020).

100. Leung, T., Kao, C., Su, W., Feng, Y. J. & Chan, C. Relationship between surface dipole, work function and charge transfer: Some exceptions to an established rule. *Phys. Rev. B* **68**, 195408 (2003).

101. Schueller, E. C. *et al.* Crystal Structure Evolution and Notable Thermal Expansion in Hybrid Perovskites Formamidinium Tin Iodide and Formamidinium Lead Bromide. *Inorg. Chem.* **57**, 695–701 (2018).

102. Fleming, R. M. *et al.* Diffraction Symmetry in Crystalline, Close-Packed C_{60}. *MRS Proc.* **206**, 691 (1990).

103. Bellaiche, L. & Vanderbilt, D. Virtual crystal approximation revisited: Application to dielectric and piezoelectric properties of perovskites. *Phys. Rev. B* **61**, 7877–7882 (2000).

104. Ramer, N. J. & Rappe, A. M. Virtual-crystal approximation that works: Locating a compositional phase boundary in $Pb(Zr_{1-x}Ti_x)O_3$. *Phys. Rev. B* **62**, R743–R746 (2000).

This project has received funding from the European Union's Horizon 2020 research and innovation programme under **Grant Agreement No. 862656**.

105.Ferreira, L. G., Marques, M. & Teles, L. K. Approximation to density functional theory for the calculation of band gaps of semiconductors. *Phys. Rev. B* **78**, 125116 (2008).

106.Tao, S. X., Cao, X. & Bobbert, P. A. Accurate and efficient band gap predictions of metal halide perovskites using the DFT-1/2 method: GW accuracy with DFT expense. *Sci. Rep.* **7**, 14386 (2017).

107.Umari, P., Mosconi, E. & De Angelis, F. Relativistic GW calculations on $CH_3NH_3PbI_3$ and $CH_3NH_3SnI_3$ perovskites for solar cell applications. *Sci. Rep.* **4**, 4467 (2014).

108.Mitzi, D. B. & Liang, K. Synthesis, Resistivity, and Thermal Properties of the Cubic Perovskite NH2CH=NH2SnI3and Related Systems. *J. Solid State Chem.* **134**, 376–381 (1997).

109.Liao, M. *et al.* Efficient and Stable $FASnI_3$ Perovskite Solar Cells with Effective Interface Modulation by Low-Dimensional Perovskite Layer. *ChemSusChem* **12**, 5007–5014 (2019).

110.Kováts, É., Oszlányi, G. & Pekker, S. Structure of the Crystalline C_{60} Photopolymer and the Isolation of Its Cycloadduct Components. *J. Phys. Chem. B* **109**, 11913–11917 (2005).

111.Dorset, D. L. & McCourt, M. P. Disorder and the molecular packing of C60 buckminsterfullerene: a direct electron-crystallographic analysis. *Acta Crystallogr. Sect. A* **50**, 344–351 (1994).

112.Shi, Z. *et al.* Lead-Free Organic-Inorganic Hybrid Perovskites for Photovoltaic Applications: Recent Advances and Perspectives. *Adv. Mater.* **29**, 1605005 (2017).

113.Pintschovius, L., Blaschko, O., Krexner, G. & Pyka, N. Bulk modulus of C 60 studied by single-crystal neutron diffraction. *Phys. Rev. B* **59**, 11020–11026 (1999).

114.Heiney, P. A. Structure, dynamics and ordering transition of solid C60. *J. Phys. Chem. Solids* **53**, 1333–1352 (1992).

This project has received funding from the European Union's Horizon 2020 research and innovation programme under **Grant Agreement No. 862656**.

115. Ma, Z.-Q., Pan, H. & Wong, P. K. A first-principles study on the structural and electronic properties of Sn-based organic–inorganic halide perovskites. *J. Electron. Mater.* **45**, 5956–5966 (2016).

116. Borriello, I., Cantele, G. & Ninno, D. *Ab initio* investigation of hybrid organic-inorganic perovskites based on tin halides. *Phys. Rev. B* **77**, 235214 (2008).

117. Guo, L., Tang, G. & Hong, J. Mechanical properties of Formamidinium halide perovskites $FABX_3$ ($FA=CH(NH_2)_2$; B=Pb, Sn; X=Br, I) by first-principles calculations *. *Chin. Phys. Lett.* **36**, 056201 (2019).

118. Roknuzzaman, M. *et al.* Ab initio atomistic insights into lead-free formamidinium based hybrid perovskites for photovoltaics and optoelectronics. *Comput. Mater. Sci.* **169**, 109118 (2019).

119. Laranjeira, J. & Marques, L. C60 structures: Structural, electronic and elastic properties. *Mater. Today Commun.* **23**, 100906 (2020).

120. Lu, J., Zhang, X., Zhao, X. & Zhang, L. Valence-band electronic structure of the simple-cubic C60. *Solid State Commun.* **108**, 89–92 (1998).

121. Jalali-Asadabadi, S. *et al.* Electronic structure of crystalline buckyballs: fcc-C60. *J. Electron. Mater.* **45**, 339–348 (2016).

122. Qian, X., Umari, P. & Marzari, N. First-principles investigation of organic photovoltaic materials C60, C70 , [C60]PCBM , and bis-[C60]PCBM using a many-body G0W0-Lanczos approach. *Phys. Rev. B* **91**, 245105 (2015).

123. Hayes, R. L., Ortiz, M. & Carter, E. A. Universal binding-energy relation for crystals that accounts for surface relaxation. *Phys. Rev. B* **69**, 172104 (2004).

124. Katan, C., Pedesseau, L., Kepenekian, M., Rolland, A. & Even, J. Interplay of spin–orbit coupling and lattice distortion in metal substituted 3D tri-chloride hybrid perovskites. *J. Mater. Chem. A* **3**, 9232–9240 (2015).

This project has received funding from the European Union's Horizon 2020 research and innovation programme under **Grant Agreement No. 862656**.

125.Horn, J. & Schlettwein, D. Contact formation of C60 to thin films of formamidinium tin iodide. 8 (2020) doi:10.1557/jmr.2020.263.

126.Traore, B. *et al.* A theoretical framework for microscopic surface and interface dipoles, work functions and valence band alignments in 2D and 3D halide perovskite heterostructures. *ACS nano energy letter* (2021).

127.Raj, A. *et al.* A computational approach to investigate the suitable ETL for lead-free CsGeI3 based perovskite solar cell. *Mater. Today Proc.* **47**, 1564–1569 (2021).

This project has received funding from the European Union's Horizon 2020 research and innovation programme under **Grant Agreement No. 862656**.